PHYSICAL REVIEW A **94**, 043803 (2016)

Structural sensitivity of x-ray Bragg projection ptychography to domain patterns in epitaxial thin films

S. O. Hruszkewycz,[1,*] Q. Zhang,[2,†] M. V. Holt,[3] M. J. Highland,[1] P. G. Evans,[2] and P. H. Fuoss[1]

[1]*Materials Science Division, Argonne National Laboratory, Argonne, Illinois 60439, USA*

[2]*Department of Materials Science and Engineering, University of Wisconsin Madison, Madison, Wisconsin 53706, USA*

[3]*Center for Nanoscale Materials, Argonne National Laboratory, Argonne, Illinois 60439, USA*

(Received 4 August 2016; published 4 October 2016)

Bragg projection ptychography (BPP) is a coherent diffraction imaging technique capable of mapping the spatial distribution of the Bragg structure factor in nanostructured thin films. Here, we show that, because these images are projections, the structural sensitivity of the resulting images depends on the film thickness and the aspect ratio and orientation of the features of interest and that image interpretation depends on these factors. We model changes in contrast in the BPP reconstructions of simulated $PbTiO_3$ ferroelectric thin films with meandering 180° stripe domains as a function of film thickness, discuss their origin, and comment on the implication of these factors on the design of BPP experiments of general nanostructured films.

DOI: 10.1103/PhysRevA.94.043803

I. INTRODUCTION

Over the last five years, Bragg ptychography has been developed as a coherent x-ray-diffraction imaging technique used to image extended crystals nondestructively in two and three dimensions with nanometer-scale spatial resolution and with picometer-scale sensitivity to internal lattice deformation [1–4]. Bragg projection ptychography (BPP) was specifically developed for two-dimensional (2D) structural imaging of crystalline thin films and has been used to generate projection images of lattice structure in films [3]. Recently, BPP experiments using a nanofocused hard x-ray beam yielded images of nanoscale distributions of strain in semiconductor materials [5] and domain morphology and polarization in a single-crystal ferroelectric film [6].

To date, BPP has been applied to samples in which the distribution of nanoscale features in the sample fulfills a special geometric case in which sharp boundaries separating regions of interest (i.e., domain walls or lithographically processed interfaces) are aligned with the diffraction plane. This geometric case simplifies the interpretation of reconstructed images but also imposes limitations on sample geometry. Here, we present a numerical study that explores the impact of these geometric constraints in BPP experiments of thin films with an arbitrary in-plane structure. We show that the structural sensitivity of the resulting image depends on the film thickness and the aspect ratio and orientation of the features of interest. These results enable BPP experiments to be designed for more general thin-film structural imaging applications. In this work, we focus on models of ferroelectric stripe domains related to recent experimental BPP work [6]; however, the results are general and apply to any film characteristics that give rise to contrast in BPP.

This work provides a basis for reliable and accurate interpretation of amplitude and phase in a two-dimensional coherent Bragg diffraction image reconstruction of thin crystals. In three-dimensional (3D) Bragg coherent diffraction imaging, the complex-valued image reconstruction spatially resolves the scattering structure factor, and this quantity can in turn be directly used to quantify lattice distortions in the crystal and the crystal morphology. However, 2D Bragg coherent diffraction imaging experiments (including BPP) are often experimentally simpler and more practical to implement. While simpler to perform, interpretation of the resulting images is typically more difficult. Thus, comprehensive investigations of the relationship between reconstructed Bragg projection images and sample structure are, in general, needed in order to advance 2D Bragg coherent diffraction imaging towards increasingly complex-structured nanomaterials and films. In this context, Dzhigaev *et al.* [7] have recently used simulation to investigate the limits under which quantitative strain measurements can be made with BPP of a faceted nanocrystal.

Here, we investigate the application of BPP to serpentine polar stripe domains in ferroelectric thin films with the goal of enabling future experimental studies that visualize local polarization (as opposed to lattice strain). Our results uncover surprising phenomena in the reconstructed images of thicker ferroelectric domains (i.e., abrupt truncations in amplitude in a material with constant, continuous physical density), and serve to highlight the critical importance of using modeling to guide experimental design and image interpretation in 2D Bragg coherent diffraction imaging. Such an approach will enable methods such as BPP to be extended to vastly more materials systems than have been explored with the technique to date.

II. MODELING BPP FROM FERROELECTRIC DOMAINS

BPP imaging simulations were performed for model $PbTiO_3$ ferroelectric thin films containing ideal 180° polar stripe domains [8] arranged in the domain pattern shown in Fig. 1(a). This model system is relevant because such a serpentine domain pattern is commonly observed in a series of thickness and temperature regimes for $PbTiO_3$ [9] and in other nanoscale ferroelectric thin films and superlattices [10,11]. In order to examine the sensitivity of BPP imaging to the widths

*shrus@anl.gov

†Present address: Advanced Photon Source, Argonne National Laboratory, Argonne, Illinois 60439, USA.

 ©2016 American Physical Society

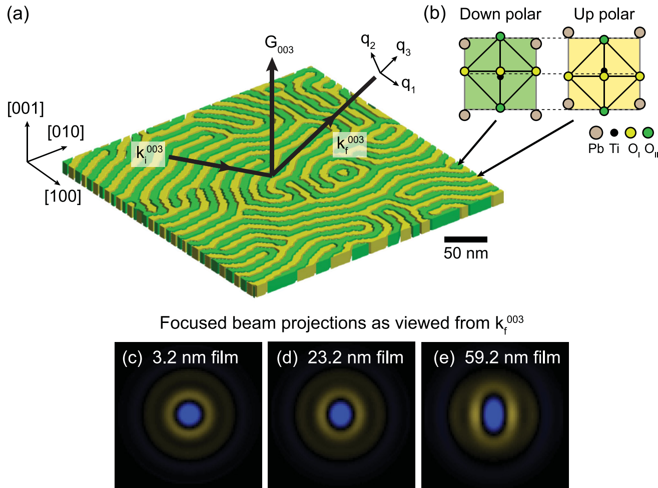

FIG. 1. (a) Simulated single-crystal ferroelectric c-axis $PbTiO_3$ thin film with serpentine stripe domains. The image shown is a space-filling depiction of the domain morphology in three dimensions in which domains oriented with polarization vectors into and out of the plane of the film are colored green and yellow, respectively. Three films, with thickness of 3.2, 23.2, and 59.2 nm, were generated using this pattern (the 23.2-nm film is shown here). Arrows indicate directions of the reciprocal-lattice vector ($\mathbf{G_{003}}$) and incident and diffracted x-ray wave vectors for the 003 x-ray Bragg reflection ($\mathbf{k_i^{003}}$, $\mathbf{k_f^{003}}$). In this formulation, it is assumed that the x rays are detected in square reciprocal space pixels, which is accurately approximated by a small area detector oriented perpendicular to $\mathbf{k_f^{003}}$. In addition, the reciprocal space coordinate system q_1, q_2, q_3 is shown. The orientation of this coordinate system was such that q_1 and q_2 lie in the plane of the area detector. (b) Atomic structure within the $PbTiO_3$ unit cell for down and up directions of the local ferroelectric remnant polarization, corresponding to the green and yellow domains in (a). (c–e) Projections of the calculated focused beam wave field (P_j^{BPP}) as projected along the $\mathbf{k_f}^{003}$ vector for each of the film thicknesses considered here.

and aspect ratios of the domains, films with thicknesses of 3.2, 23.2, and 59.2 nm were studied numerically. Real-space models of the films were generated by populating alternating domains with distorted perovskite unit cells representing the structure of a polar, coherently strained, epitaxial, c-axis $PbTiO_3$ ferroelectric film grown on a $SrTiO_3$ substrate [6,12]. In these models, the positions of atoms within the unit cells had out-of-plane displacements away from the centrosymmetric perovskite structure, as shown in Fig. 1(b), and the domain walls were oriented out of the plane.

In order to study the variation of BPP reconstructions with respect to the aspect ratio of the domain pattern, an identical domain period and spatial distribution was used for all film thicknesses. This pattern was characterized by a series of stripes with a mean period of 12 nm in which the boundaries between adjacent domains extended vertically from the top surface of the $PbTiO_3$ layer to the $SrTiO_3$ substrate. The nanoscale geometric arrangement of domains was chosen to mimic serpentine domain patterns found experimentally [13]. We note that ferroelectric serpentine domain patterns with a relationship between thickness and domain wavelength different from the Kittel-law prediction [14] (as in the simulated films presented here) have been observed in ferroelectric/dielectric superlattices [15–17].

Bragg ptychography requires a set of diffraction data measured with a localized x-ray beam rastered over the sample surface in overlapping steps (typically ∼50% overlap between neighboring positions) [18]. To generate such a set of 2D coherent nanodiffraction patterns (I_j) from a 3D model of a ferroelectric thin film illuminated with a nanofocused x-ray beam, we use the projection formalism outlined in Ref. [19] at each probe position j:

$$I_j = |\mathcal{F}\mathcal{R}(P_j \times F_{\mathrm{HKL}})|^2. \tag{1}$$

In this equation, F_{HKL} is the 3D spatially resolved structure factor of the crystal diffracting at a Bragg condition designated by reciprocal space lattice units HKL, P_j is the 3D focused beam wave field at position j, $\mathcal{R}$ is a projection operator that acts along the $\mathbf{k_f}$ direction, and $\mathcal{F}$ is a 2D Fourier transform. In this formulation, it is assumed that the x rays are detected in square reciprocal space pixels, which is accurately approximated by a small area detector oriented perpendicular to $\mathbf{k_f^{003}}$. In the case presented here, the morphology of the stripe domains was encoded in the structure factor F_{HKL} of the model film due to the fact that the oppositely polarized 180° stripe domains scatter with different relative phases at the 003 Bragg condition simulated here [6]. Thus, voxels within domains with "up"-oriented polarization were assigned a phase of 1.14 rad and unity amplitude, whereas voxels in "down"-oriented domains were assigned a phase of −1.14 rad and unity amplitude. These values correspond to the relative difference in 003 structure factor of up- and down- oriented domains in room-temperature 180° stripe domains in (001)-oriented epitaxial $PbTiO_3$ films on $SrTiO_3$ substrates [12].

The 3D focused x-ray wavefront (P_j) incident on the film was modeled after the x-ray optics at the hard x-ray nanoprobe synchrotron beamline [20,21]. The simulated focused beam from a 2.6-mrad numerical aperture Fresnel zone plate produced an intensity profile in the focal plane with a full width at half maximum of 40 nm (calculated following Ref. [22]). Simulations were conducted for an incident wave vector $\mathbf{k_i}^{003}$ corresponding to the angle satisfying the 003 Bragg condition at an x-ray wavelength of 1.23 Å ($\theta_{003} = 27.5°$). The incident and exit wave vectors for the 003 reflection are illustrated in Fig. 1(a). A side view of the scattering angles and the position of the detector relative to the Ewald sphere is also shown in Fig. 3. Scanning probe nanodiffraction patterns were generated by moving the 3D sample relative to the 3D beam in a rectangular grid of 13 × 7 points. At all points, the sample intersected the focus of the optic and a 50% beam overlap was enforced between neighboring scan points. Equation (1) was used to generate a set of intensity patterns as a function of probe position in the far-field plane of the detector (120 × 120 array of 150-μm square pixels, 0.58 m from sample).

III. ASSUMPTIONS OF THE BPP METHOD

In order to enable phase retrieval, the BPP method assumes that the projection of the probe ($\mathcal{R}P_j$) can be separated from the projection of the 3D crystal structure factor ($\mathcal{R}F_{\mathrm{HKL}}$) in Eq. (1). Thus, from the standpoint of 2D BPP image

reconstruction, Eq. (1) is approximated as

$$I_j \approx |\mathcal{F}[(\mathcal{R}P_j) \times (\mathcal{R}F_{\mathrm{HKL}})]|^2. \tag{2}$$

In this section, we examine the conditions under which the assumptions of separability underpinning this equation are valid. In the subsequent sections, we discuss a related and more critical question: under which conditions does a 2D BPP image reconstruction of $\mathcal{R}F_{\mathrm{HKL}}$ encode interpretable and quantifiable structural information about arbitrary stripe domain patterns? (a question that also extends to more general heterogeneous film structures).

We first consider the BPP probe function, which we define as $P_j^{\mathrm{BPP}} = \mathcal{R}P_j$. Without considering probe mode decomposition [23], the wavefront of the probe in a ptychography experiment should be invariant throughout the scan (outside of translation). In a BPP experiment performed at a high diffraction angle, this condition is most easily satisfied when scattering from thin films with parallel interfaces because the effective probe P_j^{BPP} is a projection of a 3D wave field through the crystal. In such a situation, P_j^{BPP} can be readily calculated [19] and will not vary as a function of position. Examples of P_j^{BPP} for the three different film thicknesses considered in this study are shown in Figs. 1(c)–1(e). In this formulation, more complex faceted crystals require that the crystal morphology be known *a priori* and that P_j is calculated separately at each sample position, thus breaking translational symmetry, so we restrict our discussion here to symmetric Bragg reflections from thin films.

With BPP, given an estimate of P_j^{BPP}, we obtain a 2D projection image of the sample ρ^{BPP} that minimizes total error with respect to the observed coherent nanodiffraction patterns at each probe position. When Eq. (1) is separable, ρ^{BPP} corresponds to $\mathcal{R}F_{\mathrm{HKL}}$. Separability, in turn, is achieved when variations of the sample structure factor F_{HKL} along the projection direction vector $\mathbf{k_f}$ are negligible. In such a case, the projection operator $\mathcal{R}$ integrates over an isostructural volume of the crystal for each imaging element, and all structural diversity along the $\mathbf{k_f}$ direction in the illuminated volume at a given probe position is encoded in P_j. The contribution from F_{HKL} in each image pixel is a complex scalar with an amplitude proportional to the thickness of the film and a phase equivalent to the structure factor of the crystal unit cell (that remains constant along the direction of integration). Because F_{HKL} does not vary along $\mathbf{k_f}$, the quantity $\mathcal{R}(P_j \times F_{\mathrm{HKL}})$ in Eq. (1) can be expressed as $(\mathcal{R}P_j) \times (nF_{\mathrm{HKL}}^{\mathrm{U.C.}})$, where n is the number of unit cells along the line of integration and $F_{\mathrm{HKL}}^{\mathrm{U.C.}}$ is the structure factor of a unit cell along this line. When F_{HKL} is isostructural along $\mathbf{k_f}$, the BPP image reconstruction ρ^{BPP} directly images $nF_{\mathrm{HKL}}^{\mathrm{U.C.}}$, which can readily be interpreted in terms of the distribution of unit-cell structure factor, and $nF_{\mathrm{HKL}}^{\mathrm{U.C.}} = \mathcal{R}F_{\mathrm{HKL}}$ under these conditions.

An isostructural integration of this sort can be enforced in two ways: (i) by ensuring that borders between differently scattering regions of the sample are parallel to the scattering plane and (ii) by imaging films with mostly 2D in-plane structure and shallow thicknesses as compared to the in-plane feature size. BPP experiments performed to date have been designed to meet these criteria and have yielded images that can be interpreted in terms of the underlying lattice structure within the thin film. Samples were chosen to satisfy the above criteria in order to ensure that the structure factor is mostly constant along the exit beam direction ($\mathbf{k_f}$). In these studies, 2D images of projected laterally varying strain fields were reconstructed in patterned semiconductor films [3,5], and local variations in polarization in linear ferroelectric domains were successfully measured [6]. Conversely, a recent numerical study of BPP from a hexagonal nanowire crystal concluded that quantitative imaging of strain fields from ρ^{BPP} of a faceted crystal with a strain field that varies along $\mathbf{k_f}$ is complicated above a certain strain threshold [7].

IV. RESULTS

With these constraints in mind, we address the following question: what aspects of the physical structure of the film can be gleaned from ρ^{BPP} when structural boundaries in the film are not aligned with the scattering plane and when the sample thickness increases relative to lateral in-plane features? We examine this question for the case of ρ^{BPP} reconstructions of serpentine ferroelectric domains in a single-crystal thin film with out-of-plane domain-wall orientation. Such a sample is more complex relative to samples studied with BPP to date, and it represents a step towards the application of BPP to more general nano- and meso-structured materials.

Using the appropriate projected beam image (P_j^{BPP}) for each film thickness [Figs. 1(c)–1(e)], the Ptychographic Iterative Engine [24] was used to reconstruct projections of the diffracted structure factor in terms of amplitude and phase (ρ^{BPP}) of each film thickness condition. Example 003 Bragg nanodiffraction patterns from the simulated data set used for these BPP reconstructions are shown in column III of Fig. 2. Calculated diffraction patterns used in the BPP reconstructions are shown from two regions of the film, one with domain boundaries that are predominantly perpendicular to the scattering plane and one in which the domains are mostly parallel to the incident beam. In these BPP reconstructions, P_j^{BPP} for each thickness was known exactly and was not refined during the course of the reconstruction (though probe refinement could be implemented [25,26]). In addition, noise-free intensity patterns were considered in order to reconstruct ρ^{BPP} at the highest available spatial resolution. The BPP results are shown in Figs. 2(a)–2(c) in terms of amplitude and phase.

Figure 2 also features an image of $\mathcal{R}F_{\mathrm{HKL}}$ calculated directly from the 3D structure factor of the polar domain pattern in the $PbTiO_3$ films projected along the $\mathbf{k_f}$ direction. In comparing the amplitudes and phases of ρ^{BPP} with $\mathcal{R}F_{\mathrm{HKL}}$, it is apparent that ρ_{HKL} replicates the major features of $\mathcal{R}F_{\mathrm{HKL}}$. The difference between ρ_{HKL} and $\mathcal{R}F_{\mathrm{HKL}}$ increases with film thickness because more variation in structure factor along $\mathbf{k_f}$ is introduced in certain areas as film thickness increases, and the approximation underpinning Eq. (2) is less valid under these conditions. Nevertheless, the amplitude and phase maps generated by BPP reconstruction and by direct projection largely mirror one other.

The more salient question then becomes: under what conditions can physically meaningful characteristics about the domain structure in the film be interpreted from a ρ^{BPP} image? The $\mathcal{R}F_{\mathrm{HKL}}$ images in Fig. 2 represent a best-case scenario for BPP phase retrieval of the domain patterns as a function

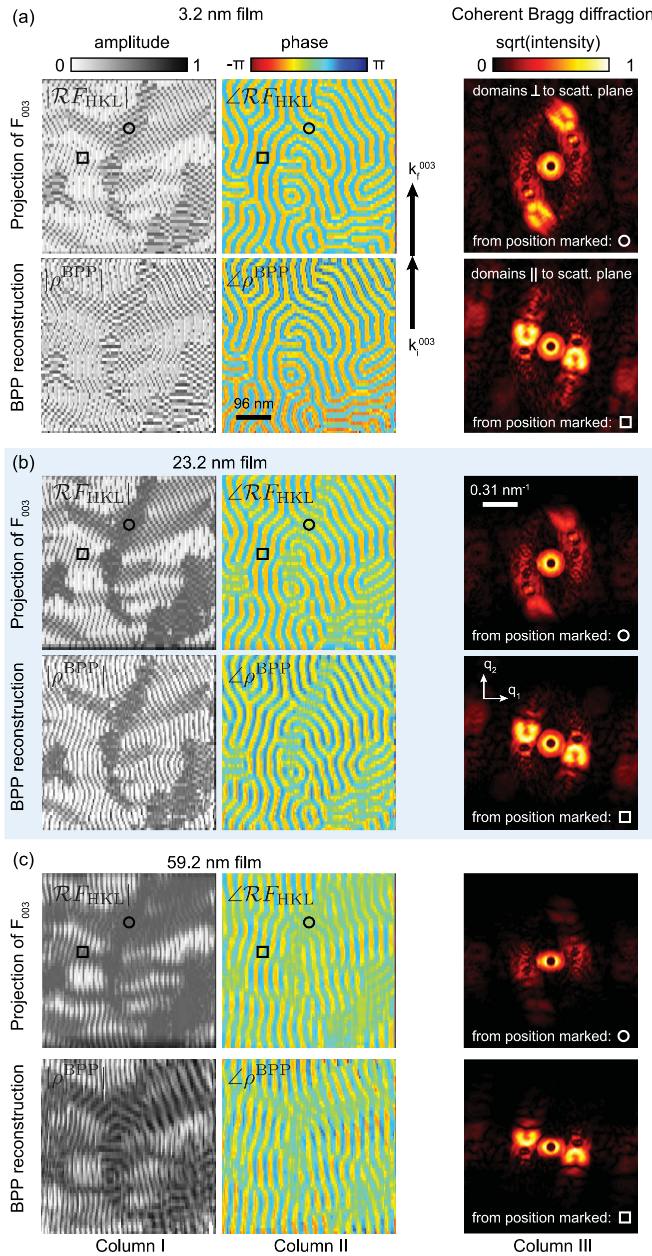

FIG. 2. Columns I and II show projections of F_{003} in terms of amplitude and phase, respectively, for simulated $PbTiO_3$ films with thicknesses of (a) 3.2, (b) 23.2, and (c) 59.2 nm. $\mathcal{R}F_{003}$ projections that were calculated directly from the model films are compared with those reconstructed by BPP (ρ^{BPP}) from simulated Bragg coherent diffraction patterns. Examples of diffraction patterns from two regions of film are given in column III corresponding to points labeled with circle and square symbols in column II. The vertical detector direction (q_2) is parallel to the scattering plane (along the 2θ direction), and the horizontal (q_1) is normal to it.

of film thickness. They contain all the structural information about the system that is retrievable with BPP.

The simulation results show clear trends as a function of thickness of the $PbTiO_3$ layer. In the 3.2-nm-thick film, the projected F_{003} amplitude is uniform to a large degree, and the phase of the stripes is well resolved and in agreement with the expected phases of the alternating stripes (± 1.14 rad) regardless of their in-plane orientation. However, areas of the film where the domain walls are perpendicular to the scattering plane show pronounced striping in the amplitude as well as more poorly resolved phase contrast. This effect becomes more pronounced as the film thickness increases. In this case, the fidelity of domains oriented away from the scattering plane further deteriorates. At a film thickness of 59.2 nm, only regions of the sample where domains are oriented within a few degrees of the scattering plane show amplitude and phase contrast comparable to the thin 3.2-nm sample. In all other regions of the thickest sample, the underlying structural details of the sample are obscured.

We also note that in the case that the film is thick enough that the path length of the incident beam through the film is comparable to the absorption or diffraction extinction lengths of the crystal, then the BPP reconstruction will not correspond fully with the projection image of the structure factor. Under such conditions, the probe intensity drops appreciably as it penetrates the material, and scattering features near the top interface of the film will contribute more strongly to the resulting diffraction patterns (and subsequent image reconstruction) than features near the substrate. However, at hard x-ray energies these lengths are of the order of several microns in typical materials, well away from the thin-film kinematic scattering regime considered here.

V. DISCUSSION AND CONCLUSION

The reduction of contrast observed in ρ^{BPP} and $\mathcal{R}F_{\mathrm{HKL}}$ in the thicker films occurs due to geometric effects. The contrast deterioration can be understood both in terms of film thickness effects in the diffraction patterns and in terms of the domain aspect ratio and orientation at a given exit beam angle. We discuss both interpretations here, and, in this light, we comment on the design of BPP imaging experiments of nanostructured thin films.

When considering films with thicknesses of only several unit cells, the projection $\mathcal{R}$ occurs over a very shallow depth, and the geometry approaches a surface reflection ptychography experiment in which all in-plane features are preserved [27,28]. In such an experiment, the average scattering pattern from the domains in the film will form a uniform-intensity halo about the Bragg peak in the detector. Similarly, a focused beam nanodiffraction experiment from a very thin $PbTiO_3$ film will encode information from all domain orientations equally in the detector. This case is exemplified in the scattering patterns in Fig. 2(a). A ring of scattering (elongated along q_2 due to the intersection of the detector and Ewald sphere) is present about the Bragg peak (the annulus in the center of the detector). The presence of strong satellite peaks reflects the orientation and spacing of the local domains illuminated at a given beam position.

As the film thickness increases from 3.2 to 59.2 nm, the effect of film thickness on the coherent diffraction pattern becomes more pronounced. The finite size of the film in the out-of-plane direction (along the direction of the crystal truncation rod) introduces a modulation of the coherent intensity pattern of the form $\sin(q)/q$ [29]. This intensity-modulating envelope acts along the surface-normal direction (along the

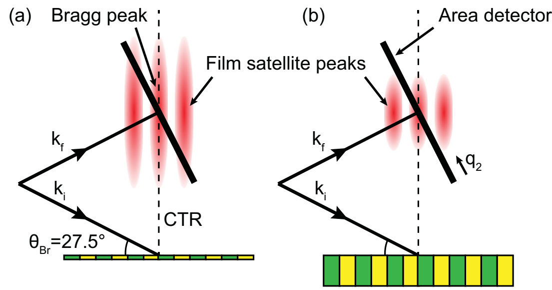

FIG. 3. Thin-film satellite peaks near a Bragg reflection are depicted from periodic structure in the film oriented perpendicular to the scattering plane. (a) Thin films, in which the diffuse scattering is distributed in an extended rod along a direction normal to the surface (along the crystal truncation rod, CTR). (b) Thicker films have a narrower distribution of intensity in the CTR direction. The thickness of the film will affect the observed intensity of the satellite peaks in the detector along the q_2 detector direction.

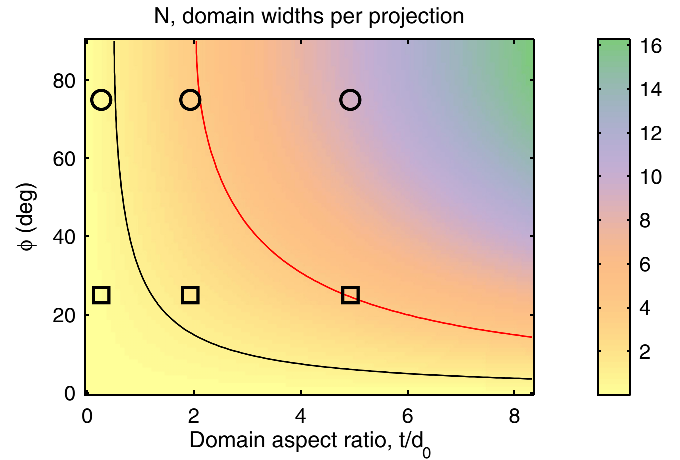

FIG. 4. A contour map is shown as a function of film thickness t and degree of domain-wall orientation ϕ relative to the scattering plane for thin-film $PbTiO_3$ domains with vertical domain walls. Here, the number of domains N projected in a given pixel is shown for a domain width of $d_0 = 12$ nm and an exit beam angle of $\theta_{Br} = 27.5°$ that defines the projection plane. Circles and squares correspond to regions of the $PbTiO_3$ model indicated in Fig. 2. The black and red contour lines correspond to values of $N = 1,4$ respectively.

crystal truncation rod) and is inversely proportional to film thickness. Thus, as depicted in Fig. 3, the intensity of satellite peaks along q_2 is increasingly modulated and damped by this envelope function as the film thickness increases. In a BPP data set that is measured at a fixed Bragg angle, information about domains oriented normal to the scattering plane is encoded along this q_2 direction of the detector. As a result, structural information about such domains in this material is very weakly encoded in thicker films (>30 nm) due to crystal truncation rod modulation of the satellite peaks.

This effect can be seen when considering the nanodiffraction patterns in Fig. 2. In Fig. 2(a), the Bragg peaks are surrounded by a pair of ordered satellite peaks. For the 3.2-nm thick film, the satellite peaks in the diffraction pattern from the region of the film with domain walls oriented perpendicular to the scattering plane (circular mark) are nearly as intense as those from the region where domains are aligned parallel to the scattering plane (square mark). With thicker films, very little information about domains oriented perpendicular to the scattering plane is encoded in the data set. Thus, in a BPP imaging experiment, the corresponding regions of the film will appear as weakly scattering (low amplitude), and with weak, ill-defined phase contrast. By contrast, the domains aligned with the scattering plane do not suffer from this effect because the thickness-dependent envelope function acts only along q_2 and not q_1 at a symmetric Bragg peak, so scattering from parallel-aligned domains is not damped for all film thicknesses.

Alternatively, one can explain this phenomenon in real space by considering the number of projected domain walls in a given area of a BPP reconstruction ρ^{BPP}. This metric quantifies the degree to which the $\mathbf{k_f}$ projection within a local volume is isostructural. In the case of the $PbTiO_3$ ferroelectric films considered here, this metric depends primarily on the aspect ratio of the domains and their local alignment with respect to the scattering plane at a given Bragg angle. Figure 4 shows the number of projected domains in a given volume (N) as a function of domain aspect ratio (t/d_0) and domain orientation angle (ϕ) at a symmetric Bragg angle of 27.5°. A value of $\phi = 0$ corresponds to domain walls that are parallel to the scattering plane, t denotes the out-of-plane film thickness, and d_0 is the average in-plane domain width. Red and black curves are equal-N contours for $N = 1,4$ domains, respectively. Also shown on the plot are the two regions of ρ^{BPP} considered in Fig. 2 (circle and square markers) for film thicknesses of 3.2, 23.2, and 59.2 nm.

These curves can be considered as a two-level criterion for resolving meandering stripes in $PbTiO_3$ with BPP. Maintaining a value of $N < 1$ (black contour) for all in-plane domain orientations ϕ present in the film ensures that the phase contrast of the stripe domains in ρ^{BPP} is at least 90% of the $PbTiO_3$ structure factor phase of an up- or down-polarized unit cell within a given domain. In this regime, the phase of ρ^{BPP} can be directly converted to quantify the local polarization in the film. The red contour represents ∼50% phase contrast accuracy in ρ^{BPP} relative to the unprojected structure factor values (estimates of phase contrast accuracy based on analysis of line cuts through $\angle \mathcal{R} F_{HKL}$ in Fig. 2).

These criteria can be used to plan BPP experiments that produce images for different types of analysis. For example, full quantification of the local out-of-plane polarization within individual ferroelectric domains (as demonstrated experimentally in Ref. [6]) requires phase contrast in ρ^{BPP} that can directly be related to the underlying lattice structure, i.e., $N < 1$. For this reason, the experiment in Ref. [6] was designed and performed such that $N \sim 0.6$ was maintained for a 25-nm-thick $PbTiO_3$ film with 11-nm-wide 180° ferroelectric strip domains. On the other hand, studies that emphasize uncovering the domain *morphology* rather than polarization, for example, in the buried layers of a ferroelectric device or superlattice [30], can be designed to maintain $N \sim 4$ via a combination of domain width, domain orientation, layer thickness, and Bragg scattering angle.

The quantity ρ^{BPP} closely approximates a fixed-angle projection of the structure factor of the sample at a given

Bragg condition. The geometric details of this projection with respect to the features of interest in the film must be understood in order to extract meaningful physical properties about the sample from the resulting image. We note that, though the above discussion focused on 180° stripe domains in $PbTiO_3$ films, the concepts presented are general and apply to BPP experiments of various nanostructured films, including those with internal strain fields. In this light, we conclude that careful consideration must be given to the design of BPP experiments, and that projections of structural models of the sample are often necessary for interpreting the contrast of a BPP image. This is especially true for complex nanostructured thin films that deviate from an isostructural projection along the exit beam direction. Enabling such an imaging capability opens the door to *in situ* studies of nanostructured films under working conditions that can capitalize on the order-of-magnitude improvements in brightness at next-generation synchrotron sources being commissioned worldwide [31].

ACKNOWLEDGMENTS

Ptychographic simulations and generation of reconstructions were supported by the U.S. Department of Energy, Office of Science, Basic Energy Sciences, Materials Sciences and Engineering Division. Geometric algorithms for the simulation of the nanodomain arrangement were developed at University of Wisconsin-Madison under support from U.S. Department of Energy, Basic Energy Sciences, Materials Sciences and Engineering Division under Contract No. DE-FG02-04ER46147. Use of the Center for Nanoscale Materials was supported by the U.S. Department of Energy, Office of Science, Office of Basic Energy Sciences, under Contract No. DE-AC02-06CH11357.

[1] P. Godard, G. Carbone, M. Allain, F. Mastropietro, G. Chen, L. Capello, A. Diaz, T. H. Metzger, J. Stangl, and V. Chamard, Nat. Commun. **2**, 568 (2011).
[2] Y. Takahashi, A. Suzuki, S. Furutaku, K. Yamauchi, Y. Kohmura, and T. Ishikawa, Phys. Rev. B **87**, 121201 (2013).
[3] S. O. Hruszkewycz, M. V. Holt, C. E. Murray, J. Bruley, J. Holt, A. Tripathi, O. G. Shpyrko, I. Mcnulty, M. J. Highland, and P. H. Fuoss, Nano Lett. **12**, 5148 (2012).
[4] A. I. Pateras, M. Allain, P. Godard, L. Largeau, G. Patriarche, A. Talneau, K. Pantzas, M. Burghammer, A. A. Minkevich, and V. Chamard, Phys. Rev. B **92**, 205305 (2015).
[5] M. V. Holt, S. O. Hruszkewycz, C. E. Murray, J. R. Holt, D. M. Paskiewicz, and P. H. Fuoss, Phys. Rev. Lett. **112**, 165502 (2014).
[6] S. O. Hruszkewycz, M. J. Highland, M. V. Holt, D. Kim, C. M. Folkman, C. Thompson, A. Tripathi, G. B. Stephenson, S. Hong, and P. H. Fuoss, Phys. Rev. Lett. **110**, 177601 (2013).
[7] D. Dzhigaev, T. Stankevic, I. Besedin, S. Lazarev, A. Shabalin, M. N. Strikhanov, R. Feidenhans'l, and I. A. Vartanyants, Proc. SPIE **9592**, 95920S (2015).
[8] S. K. Streiffer, J. A. Eastman, D. D. Fong, C. Thompson, A. Munkholm, M. V. Ramana Murty, O. Auciello, G. R. Bai, and G. B. Stephenson, Phys. Rev. Lett. **89**, 067601 (2002).
[9] D. D. Fong, A. M. Kolpak, J. A. Eastman, S. K. Streiffer, P. H. Fuoss, G. B. Stephenson, C. Thompson, D. M. Kim, K. J. Choi, C. B. Eom, I. Grinberg, and A. M. Rappe, Phys. Rev. Lett. **96**, 127601 (2006).
[10] M. Dawber, N. Stucki, C. Lichtensteiger, S. Gariglio, P. Ghosez, and J. M. Triscone, Adv. Mater. **19**, 4153 (2007).
[11] D. G. Schlom, L.-Q. Chen, C.-B. Eom, K. M. Rabe, S. K. Streiffer, and J.-M. Triscone, Annu. Rev. Mater. Res. **37**, 589 (2007).
[12] B. Meyer and D. Vanderbilt, Phys. Rev. B **65**, 104111 (2002).
[13] C. Thompson, D. D. Fong, R. V. Wang, F. Jiang, S. K. Streiffer, K. Latifi, J. A. Eastman, P. H. Fuoss, and G. B. Stephenson, Appl. Phys. Lett. **93**, 182901 (2008).
[14] C. Kittel, Rev. Mod. Phys. **21**, 541 (1949).
[15] P. Zubko, N. Stucki, C. Lichtensteiger, and J.-M. Triscone, Phys. Rev. Lett. **104**, 187601 (2010).
[16] J. Y. Jo, P. Chen, R. J. Sichel, S. J. Callori, J. Sinsheimer, E. M. Dufresne, M. Dawber, and P. G. Evans, Phys. Rev. Lett. **107**, 055501 (2011).
[17] P. Zubko, N. Jecklin, A. Torres-Pardo, P. Aguado-Puente, A. Gloter, C. Lichtensteiger, J. Junquera, O. Stéphan, and J. M. Triscone, Nano Lett. **12**, 2846 (2012).
[18] O. Bunk, M. Dierolf, S. Kynde, I. Johnson, O. Marti, and F. Pfeiffer, Ultramicroscopy **108**, 481 (2008).
[19] S. O. Hruszkewycz, M. V. Holt, M. Allain, V. Chamard, S. M. Polvino, C. E. Murray, and P. H. Fuoss, Opt. Lett. **40**, 3241 (2015).
[20] M. Holt, R. Harder, R. Winarski, and V. Rose, Annu. Rev. Mater. Res. **43**, 183 (2013).
[21] S. O. Hruszkewycz, M. V. Holt, J. Maser, C. E. Murray, M. J. Highland, C. M. Folkman, and P. H. Fuoss, Phil. Trans. R. Soc. A **372**, 20130118 (2014).
[22] S. O. Hruszkewycz, M. V. Holt, A. Tripathi, J. Maser, and P. H. Fuoss, Opt. Lett. **36**, 2227 (2011).
[23] M. Odstrcil, P. Baksh, S. A. Boden, R. Card, J. E. Chad, J. G. Frey, and W. S. Brocklesby, Opt. Express **24** 8360 (2016).
[24] H. M. L. Faulkner and J. M. Rodenburg, Phys. Rev. Lett. **93**, 023903 (2004).
[25] P. Thibault, M. Dierolf, O. Bunk, A. Menzel, and F. Pfeiffer, Ultramicroscopy **109**, 338 (2009).
[26] A. M. Maiden and J. M. Rodenburg, Ultramicroscopy **109**, 1256 (2009).
[27] D. F. Gardner, B. Zhang, M. D. Seaberg, L. S. Martin, D. E. Adams, F. Salmassi, E. Gullikson, H. Kapteyn, and M. Murnane, Opt. Express **20**, 19050 (2012).
[28] S. Marathe, S. S. Kim, S. N. Kim, C. Kim, H. C. Kang, P. V. Nickles, and D. Y. Noh, Opt. Express **18**, 7253 (2010).
[29] P. Fuoss and S. Brennan, Annu. Rev. Mater. Sci. **20**, 365 (1990).
[30] A. K. Yadav, C. T. Nelson, S. L. Hsu, Z. Hong, J. D. Clarkson, C. M. Schlepuetz, A. R. Damodaran, P. Shafer, E. Arenholz, L. R. Dedon, D. Chen, A. Vishwanath, A. M. Minor, L. Q. Chen, J. F. Scott, L. W. Martin, and R. Ramesh, Nature (London) **530**, 198 (2016).
[31] M. Borland, G. Decker, L. Emery, V. Sajev, Y. Sun, and A. Xiao, J. Synchrotron Rad. **21**, 912 (2014).